# $CHD_3$ Dissociation on the Kinked Pt(210) Surface: A Comparison of Experiment and Theory

*Helen Chadwick[1†*], Ana Gutiérrez-González[2], Rainer D. Beck[2] and Geert-Jan Kroes[1]*

1. Leiden Institute of Chemistry, Gorlaeus Laboratories, Leiden University, P.O. Box 9502, 2300 RA Leiden, The Netherlands.

2. Laboratoire de Chimie Physique Moléculaire, Ecole Polytechnique Fédérale de Lausanne, CH-1015 Lausanne, Switzerland.

ABSTRACT

To be able to simulate activated heterogeneously catalyzed reactions on the edge and corner sites of nanoparticles, a method for calculating accurate activation barriers for the reactions is required. We have recently demonstrated that a semi-empirical specific reaction parameter (SRP) density functional developed to describe $CHD_3$ dissociation on a flat Ni(111) surface is transferable to describing the same reaction on a stepped Pt(211) surface. In the current work, we compare initial sticking coefficients measured using the King and Wells beam reflectivity technique and calculated from *ab-initio* molecular dynamics trajectories using the same SRP functional for $CHD_3$ dissociation on a kinked Pt(210) surface at a temperature of 650 K. The calculated sticking coefficients overestimate those determined experimentally, with an average energy shift between the two curves of 13.6 kJ/mol, which is over a factor of three times higher than the 4.2 kJ/mol limit that defines chemical accuracy. This suggests the SRP functional predicts an activation barrier that is too low for the dissociation on the least coordinated kink atom, which is the site of the lowest energy transition state and where most of the dissociation occurs in the calculations.

## 1. Introduction

Methane dissociation is one of the elementary reaction steps in the steam reforming[1–3] and dry reforming processes[4–6], both of which are used to make syngas on an industrial scale. *In-situ* measurements have shown that nanoparticles which typically catalyze these reactions have areas of well-defined surface planes separated by edges and corners[7–10], with most of the reactivity expected to occur on these defect sites[11–13]. If the nanoparticles are large enough and the screening effects of the mobile electrons sufficient, then they can be considered to be made of independent sites where the properties are not influenced by the nanoparticle geometry more than a few Å away[14]. As such, the defect sites can be modelled in surface science studies by using surfaces with kinks and steps to model the effects of corners and edges, for example both Ni(211) and Pt(211) have previously been used to study the effect of line defects in methane dissociation[15–18].

The differences in activation barrier seen for flat and defected surfaces can be due to two effects; geometric and electronic[14]. For the dissociation of methane the change in activation barrier has been shown to mostly be an electronic effect, as the transition state is located above a single metal atom[14]. Transition state scaling relationships have shown that the activation barriers tend to scale linearly with adsorption energies for adsorbates on different sites of transition metal surfaces[19–21]. In addition, Calle-Vallejo et al. have shown that adsorption energies tend to scale linearly with the generalized co-ordination number[22,23]. This is a variation on the co-ordination number which also takes into account the number of nearest neighbor atoms of the neighboring atom of interest. It follows that the activation barriers generally scale linearly with the generalized co-ordination number. Calculated values of activation barriers for methane dissociation do tend to be lower for kink and step defects than for flat transition metal surfaces[24–26].

Experimental studies have also shown the influence of the surface structure on the dissociation of methane on (group 10) transition metals. Beebe et al. showed that the dissociation probabilities, or initial sticking coefficients, for methane reacting under thermal conditions on low index nickel surfaces increases in the order Ni(111) < Ni(100) < Ni(110)[27]. The reactivity of a Ni(111) surface which was sputtered but not annealed, which introduces defects to the surface, was shown to be higher than for the annealed surface by Egeberg et al.[28]. In addition, studies which used gold[28] or sulfur[29] to passivate defect sites present on Ni(111) surfaces observed lower reaction probabilities than on a clean (unpassivated) Ni(111) surface, demonstrating the higher reactivity of the defect sites. Klier et al.[30] made a direct comparison between kinked, stepped and flat palladium surfaces, and found that the sticking coefficients for methane dissociation under thermal conditions on the kinked Pd(679) surface measured by Wang et al.[31] were larger than their values for the reactivity on the stepped Pd(311) surface which in turn were larger than the values they obtained for the flat Pd(111) surface[30].

An earlier study by Gee et al. demonstrated that the initial sticking coefficients for methane dissociation on the stepped Pt(533) surface were larger than those on a flat Pt(111) surface[32]. Our recent joint experimental-theoretical studies support this conclusion, having shown that the initial sticking coefficients for $CHD_3$ dissociation on Pt(111) are smaller than for the stepped Pt(211) and Pt(110)-(2x1) surfaces at incident energies up to 100 kJ/mol[33], due to the activation barrier for dissociation being higher on Pt(111) than on the step edges of Pt(211)[15,34] and ridge atoms of Pt(110)-(2x1)[33]. In addition, reflection absorption infrared spectroscopy experiments have confirmed that at low incident energies, all detectable methane dissociation on Pt(211) occurs on the least coordinated step edge atoms[35,36]. On Pt(110)-(2x1), all detectable methane dissociation occurs on the least coordinated ridge atoms even at higher incident energies[37].

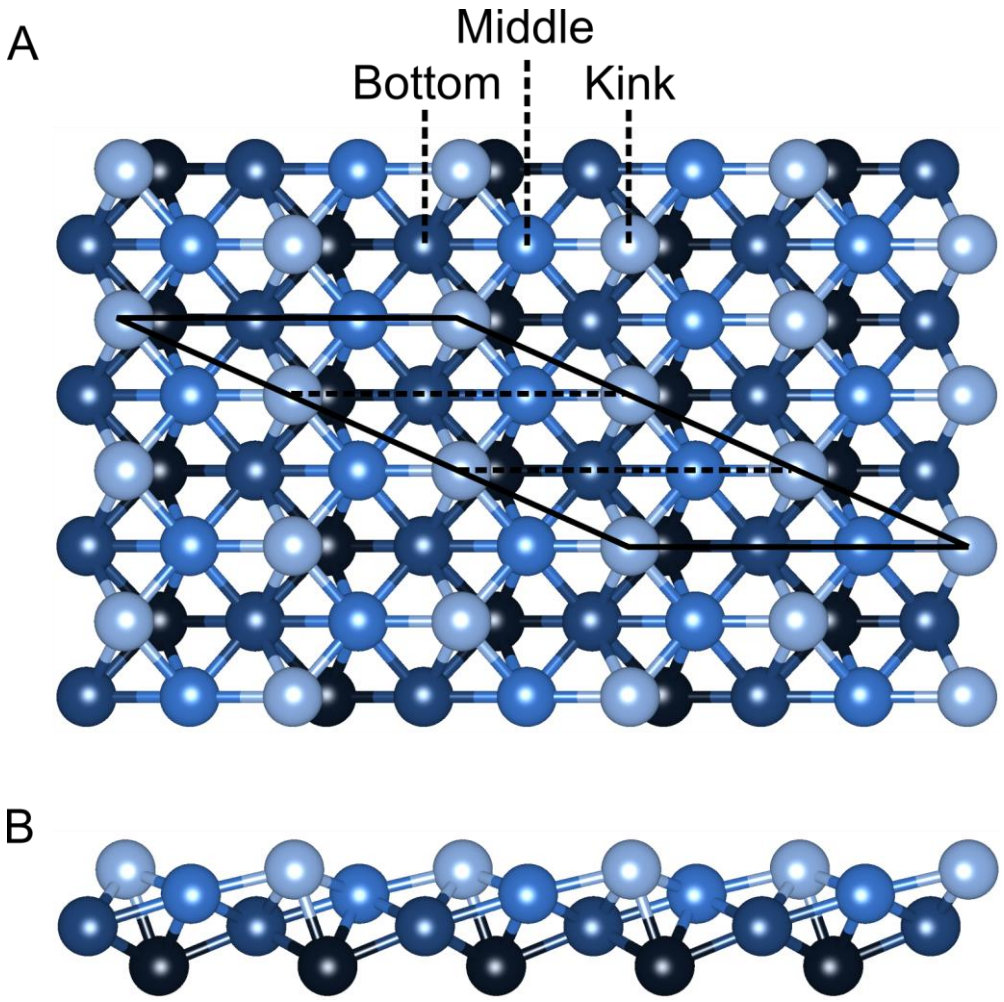


**Figure 1.** Panel A: Schematic top view of the Pt(210) surface. The surface is made from three different atoms, which we refer to as kink, middle and bottom, with the kink atoms being the highest, and the bottom the lowest. The solid lines show the (3x1) supercell used in the calculations, and the dashed lines the unit cell. Panel B: Schematic side view of the Pt(210) surface.

The above studies show the important role played by kink and line defects in the dissociation of methane on transition metal surfaces. It follows that any theoretical description of the reaction must also be able to accurately model methane dissociation on defect sites. By using specific reaction parameter density functional theory (SRP-DFT) we have already shown that the same SRP functional (SRP32-vdW) can accurately reproduce sticking coefficients for $CHD_3$ dissociation on Ni(111)[38,39], Pt(111)[15] and Pt(211)[15,35,40] for a range of incident energies and rovibrational states. This has demonstrated that the SRP32-

vdW functional is transferable among systems in which methane interacts with flat nickel and platinum surfaces, and the stepped Pt(211) surface. However, it underestimated the sticking coefficients for $CHD_3$ dissociation on Pt(110)-(2x1), as it failed to capture the geometry of the surface correctly which led to the calculated activation barrier being up to 10 kJ/mol too high[33]. In the present work we will compare results from King and Wells measurements and *ab-initio* molecular dynamics (AIMD) calculations to determine if the SRP32-vdW DF is also able to quantitatively reproduce the reactivity on the kinked Pt(210) surface. The structure of the Pt(210) surface is shown schematically in Figure 1. There are three different atomic sites in the surface, which we refer to as kink, middle and bottom, as shown in Figure 1A.

The rest of the paper is organized as follows. In Sections 2 and 3 we describe the theoretical and experimental methods that are employed in the current work. In Section 4, we present the results and discussion before the summary in Section 5.

## 2. Theoretical Methods

The setup of the AIMD calculations and sampling of the initial conditions have been described in detail previously[15,38] and only a brief overview will be presented here. At each incident energy, $\langle E_i \rangle$, either 500 or 1000 trajectories were run at normal incidence for $CHD_3$ hitting a Pt(210) surface at a surface temperature of 650 K. The quasi-classical AIMD trajectories were run using the Vienna *ab-initio* simulation package (VASP) version 5.3.5[41–44]. The Pt(210) surface was modelled using a (3x1) supercell shown by the solid lines in Figure 1A with thirteen atomic layers, with the bottom three layers held fixed in their bulk position. A cut off energy of 400 eV (1 eV ≈ 96.5 kJ/mol) has been used for the plane wave basis set, with a 0.1 eV (≈ 9.6 kJ/mol) wide Fermi smearing to facilitate convergence. The core electrons were represented using a projector augmented wave (PAW) method[45,46] with the pseudopotentials calculated using the PBE functional[47,48]. A 3 x 4 x 1 Γ-centered K-point

grid was used to sample the first Brillouin zone. Extensive tests of these parameters have been performed as detailed in Section S2 of the Supporting Information (SI).

As in previous work for $CHD_3$ dissociation on nickel[15,38], platinum[15,25,33,40] and copper surfaces[49], we make use of the semi-empirical SRP32-vdW exchange correlation functional defined as

$$SRP32 - vdW = (1 - 0.32)E_X^{PBE} + 0.32E_X^{RPBE} + E_C^{vdW} \quad (1)$$

where $E_X^{PBE}$ and $E_X^{RPBE}$ are the PBE[47,48] exchange and RPBE[50] exchange functionals, and $E_C^{vdW}$ is the van der Waals correlation functional of Dion et al.[51,52].

The initial $XY$ position of the COM of the $CHD_3$ was randomly sampled over the area of the super cell, and $Z$ was fixed at 6.5 Å above the Pt(210) surface. The velocity of the molecule was sampled from the experimental velocity distribution used to measure the sticking coefficients of $CHD_3$ on Pt(111) (see Table S2 of Reference 15) or those determined from the Pt(210) measurements. As detailed in Section S3 and following the procedures used in previous work[15,33,38,40,49], 1.9 kJ/mol was added to the kinetic energy to account for the residual energy due to the 13 Å vacuum spacing used between periodic replicas in the AIMD calculations. The trajectories were run in a quasi-classical framework meaning that zero point energy is added to the vibrational modes of the $CHD_3$. For the laser-off calculations, the vibrational states of the molecule were randomly populated according to a Boltzmann distribution for the nozzle temperature used to generate the molecular beam expansion and the initial orientation of the molecule chosen randomly. For the $v_1 = 1$ calculations, the molecule was prepared in the $J$ = 2, $K$ = 1, $v_1 = 1$ rovibrational state, with the $M$ = -2, -1, 0, 1 and 2 levels sampled equally as the molecular flight time between the laser and the surface in the experiments on other platinum surfaces[15] is on the order of a few hundred μs so any initial alignment created by the laser excitation would be lost due to hyperfine coupling[53]. The initial velocities and positions of the atoms in the Pt(210) were randomly selected from

AIMD calculations run to equilibrate the surface at 650 K, as described in Section S1 of the SI.

The trajectories were propagated with a time step of 0.4 fs using the Velocity-Verlet algorithm as implemented in VASP until they were determined to have either reacted, scattered or trapped. A trajectory was considered to have reacted if one of the bonds in the molecule became larger than 3 Å or was longer than 2 Å for 100 fs, whereas a trajectory scattered when the center of mass (COM) was at a height of 6.5 Å above the Pt(210) plane and the COM velocity was directed away from the surface. If none of these outcomes were reached within a propagation time of 1 ps, the trajectory was considered to be trapped on the surface.

The reaction probability ($p_\mathrm{i}$) was calculated as

$$p_\mathrm{i} = \frac{N_\mathrm{react}}{N_\mathrm{tot}} \tag{2}$$

where $N_\mathrm{react}$ is the number of trajectories that react, and $N_\mathrm{tot}$ the total number of trajectories that were run for a given incident energy. The errors were calculated as

$$\sigma_\mathrm{i} = \sqrt{\frac{p_\mathrm{i}(1-p_\mathrm{i})}{N_\mathrm{tot}}} \tag{3}$$

and represent 68% confidence limits. The other probabilities and associated errors presented here were calculated with analogous expressions, unless the probability is 0 or 1, in which case the error was calculated using[54]

$$\sigma_\mathrm{i} = 1 - 0.32^{1/N_\mathrm{tot}} \tag{4}$$

## 3. Experimental Methods

The experiments were performed in a molecular beam-surface science apparatus that has been described in detail previously[55]. Briefly, the apparatus consists of a triply differentially pumped molecular beam source coupled to an ultra-high vacuum (UHV) chamber with a base pressure of 5 x $10^{-11}$ mbar where the Pt(210) sample is located.

The $CHD_3$ continuous molecular beam was formed by expanding a 1.7% $CHD_3$ in $H_2$ mixture through a 50 μm-diameter nozzle hole into the molecular beam source chamber. The translational energy of the $CHD_3$ molecules was varied by heating the nozzle between 300 and 600 K, yielding average translational energies in the range between 69 and 118 kJ/mol with an average distribution width $\Delta E_i/E_i = 0.25$ as determined by a time-of-flight method using a chopper wheel in combination with an on-axis quadrupole mass spectrometer (QMS).

The Pt(210) surface sample (Surface Preparation Labs) of 10 mm diameter was mounted between two tungsten wires attached to a liquid nitrogen cryostat. The surface temperature ($T_S$) was controlled between 90 and 1200 K using nitrogen cooling and by passing a DC current through the tungsten wires to heat the sample. In all the experiments reported here, $CHD_3$ depositions were performed at $T_S = 650$ K, which is above the desorption temperature of $H_2$ and CO. This prevents any site blocking by adsorption of residual CO from the UHV background and quickly removes any H and D atoms formed by $CHD_3$ dissociation from the surface by recombinative desorption.

Surface cleaning between experiments was performed by $Ar^+$ sputtering followed by annealing the sample at 1100K in UHV. After annealing, the surface was cooled at a rate of 1 K/s to avoid undergoing a roughening transition as previously observed on Pt(210) when the cooling rate was about 300 K/s[56]. The surface cleanliness was verified using Auger electron spectroscopy, confirming that no detectable (< 1% monolayer) trace of carbon or oxygen was on the surface. The surface structure after the annealing was confirmed by low energy

electron diffraction (LEED), showing the expected pattern[57] with no streaking of the peaks indicative of a disordered surface.

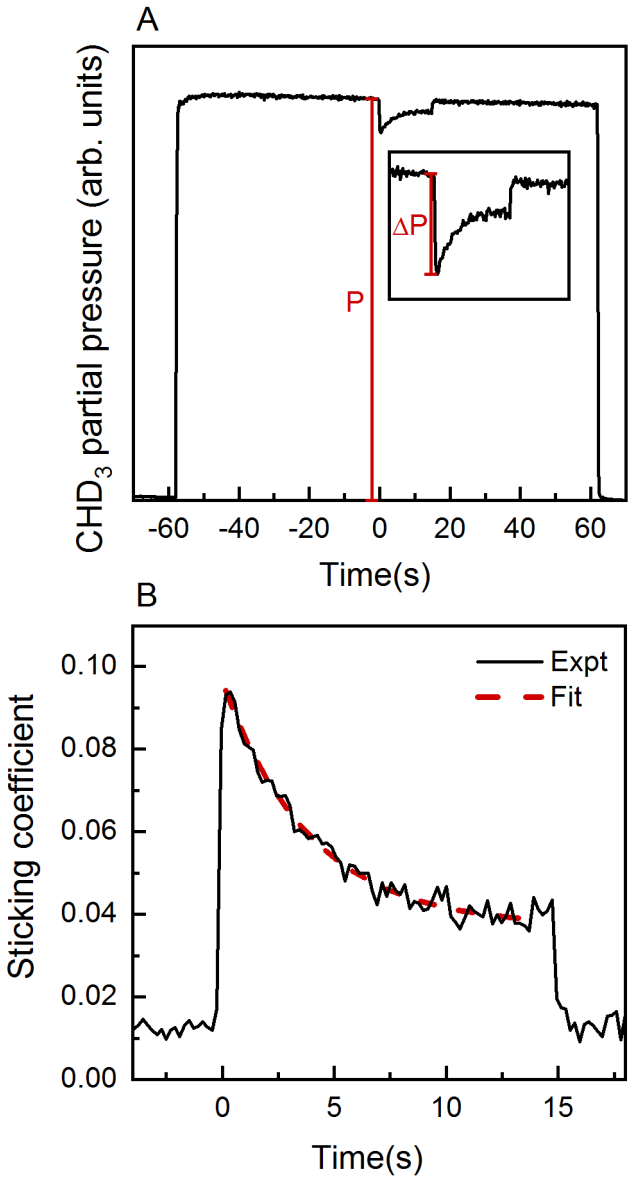


**Figure 2.** Panel A: King and Wells QMS trace for the dissociative chemisorption of $CHD_3$ on Pt(210) at an incident translational energy of 107 kJ/mol and surface temperature of 650 K. At time t = 0, the beam flag is raised and the molecular beam directly hits the Pt(210) surface. Panel B: Time dependence of the sticking coefficient calculated using eq 5. The dashed red line corresponds to the fit to the data using a double exponential decay.

The sticking coefficients were measured using the King and Wells (K&W) method[58]. A QMS was used to monitor the $CHD_3$ partial pressure in the UHV chamber at 19 amu. An example of a typical K&W measurement trace is shown in Figure 2A. The time axis has been shifted so that at $t$ = 0 the molecular beam starts to impinge on the Pt(210) crystal surface. Initially, at $t$ < -58 s, before the molecular beam enters into the UHV chamber, there is no detectable QMS signal for mass 19 amu. At $t$ = -58 s, a separation valve is opened and the molecular beam enters the UHV chamber. For the first 58 s (between $t$ = -58 s and $t$ = 0 s), an inert PTFE beam flag is inserted in the path of the molecular beam preventing the molecules from directly hitting the sample crystal. At $t$ = 0 s, the beam flag is raised, exposing the Pt(210) surface to the molecular beam. Any sticking of $CHD_3$ on the surface results in a decrease (ΔP) of the 19 amu QMS signal. The pressure drop decreases with time as the surface is being passivated by adsorbed carbon atoms. After 15 s deposition, the beam flag blocks the molecular beam again, and at $t$ = 62 s, the separation valve is closed.

The time dependent sticking coefficient $S(t)$ is given by:

$$S(t) = \frac{\Delta P(t)}{P} \tag{5}$$

where $\Delta P(t)$ is the change in the partial pressure of mass 19 amu in the QMS for t > 0 when the flag is open, and $P$ is the increase in the partial pressure of mass 19 amu when the molecular beam enters the UHV chamber. Figure 2B shows the corresponding $S(t)$ for the QMS trace shown in Figure 2A. $S(t)$ traces were fit using a double exponential decay[59] to obtain the initial sticking coefficient $S_0$ at $t$ = 0. When no reactivity was observed, the QMS current was seen to increase when the beam flag was opened, yielding a different baseline of the K&W trace when the flag is opened and closed. This effect has been accounted for in the analysis of the experimental data, and the correction yields the apparent nonzero baseline when the beam flag is closed ($t$ < 0 s, and $t$ > 15 s) in Figure 2B.

## 4. Results and Discussion

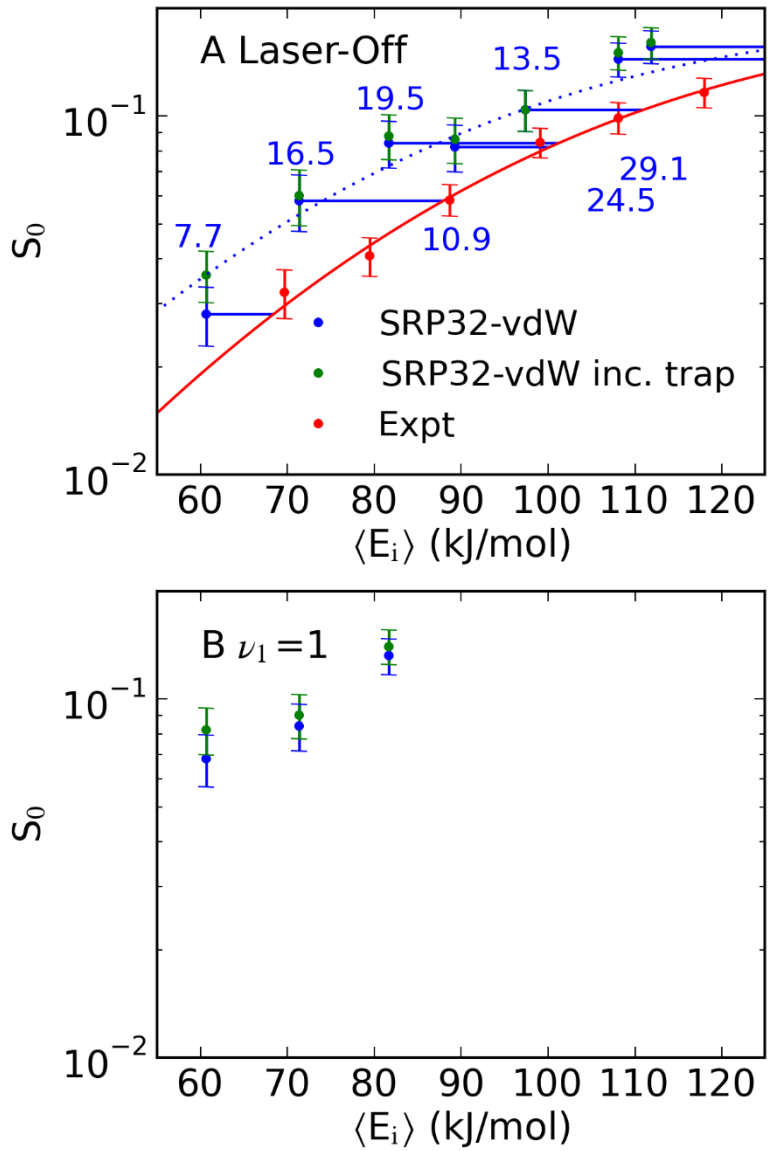


**Figure 3.** Panel A: A comparison of the sticking coefficients measured (red) and calculated from the AIMD trajectories including (green) and excluding (blue) the contribution to the reaction probability from the trapped trajectories under laser-off conditions. The red line shows an S-shape curve fit to the experimental data using eq 6, the dotted blue line the fit shifted by 13.8 kJ/mol and the blue numbers the shift (in kJ/mol) between the measured and calculated sticking coefficients. Panel B: The calculated sticking coefficients for $CHD_3$ molecules prepared with a quantum of C-H stretch vibration including (green) and excluding (blue) the contribution to the reaction probability from the trapped trajectories.

A comparison between the experimental (red) and calculated initial sticking coefficients for $CHD_3$ dissociation on Pt(210) which include (green) and exclude (blue) the contribution from the trajectories which are trapped after the 1 ps propagation time under

laser-off conditions is presented in Figure 3A. Results from AIMD calculations for molecules prepared with a quantum of C-H stretch vibration are presented in Figure 3B. For both molecules prepared in $v_1 = 1$ and under laser-off conditions the trapping probabilities are small. In the laser-off case, the calculated sticking coefficients consistently overestimate those that are obtained experimentally. To quantify the energy difference between the two sets of data, the experimental data were fit using an S-shape curve defined as[60]

$$S_0(E_i) = \frac{A}{2}\left(1 + \mathrm{erf}\left(\frac{E_i - E_0}{W}\right)\right) \quad (6)$$

$A$ corresponds to the sticking coefficient at infinitely high translational energy, $E_i$ the incident energy, $E_0$ the effective activation barrier and $W$ the effective width of the barrier heights. The values of $A$, $E_0$ and $W$ obtained from the fit to the experimental data are given in Table 1. The shift between the calculated sticking coefficients and the fit to the experimental data are shown in kJ/mol in Figure 3A. Excluding the sticking coefficients for the two highest energy calculations as these fall outside the range of experimentally determined data, the average shift between the experiments and the calculations is 13.6 kJ/mol. This is over a factor of three larger than the 4.2 kJ/mol limit which is considered to define chemical accuracy. Therefore, the SRP32-vdW functional fails to give a chemically accurate description of the experiments for $CHD_3$ dissociation on the kinked Pt(210) surface.

**Table 1.** The values of $A$, $E_0$ and $W$ used in eq 6 to obtain the fits to the experimental and calculated sticking coefficients presented Figure 3A. The parameters $A$ and $W$ were held fixed at the values from the fit to the experimental data when fitting the data from the AIMD calculations.

| | $A$ | $E_0$ (kJ/mol) | $W$ (kJ/mol) |
|---|---|---|---|
| Experiment | 0.19 | 105.6 | 50.9 |
| AIMD calculations | 0.19 | 91.8 | 50.9 |

We cannot completely rule out that the calculated and experimental sticking coefficients do not agree due to a roughening of the Pt(210) surface experimentally, which has been shown to affect other kinked platinum surfaces[61,62]. In work by Sander et al.[56], they report roughening of the Pt(210) surface, although after annealing the surface they cool at a rate of 300 K/s which is likely to be too fast to allow the surface to relax to the lowest energy structure. Other work shows that cooling the surface more slowly produces an ordered Pt(210) surface which does not reconstruct[63]. In the current study, the surface was cooled at a rate of 1 K/s and a LEED measurement taken which was in good agreement with that shown in Reference 57 for Ir(210). This confirms the long range order of the Pt(210) surface used in the experiments, although it does not exclude the possibility of roughening of the surface on a microscopic scale.

Alternatively, the structure of the Pt(210) surface may not be correctly reproduced by the SRP32-vdW functional as functionals which include van der Waals correlation do not necessarily produce the right surface geometry[64]. In recent work on Pt(110)-(2x1)[33] we found that the activation barrier for dissociation of $CHD_3$ was up to 10 kJ/mol higher when the surface structure calculated using the SRP32-vdW functional was used compared to those obtained experimentally[65–67]. A comparison of the calculated and experimental[63] Pt(210) surface geometries can be found in Table S1 of the SI. The lowest activation barrier calculated using the surface geometry determined from LEED measurements in Reference 63 was found to be 3.9 kJ/mol lower than using the 0 K geometry obtained by relaxing the Pt(210) slab using the SRP32-vdW functional (see below). Whilst this is within chemical accuracy, the lower activation barrier would lead to an increase in the calculated sticking coefficients, causing an even larger disagreement between the theoretical and experimental values of $S_0$. This suggests differences between the calculated and experimental surface

geometries are not the reason for the calculations overestimating the measured sticking coefficients.

Another potential source of disagreement between the experimental and calculated sticking coefficients might be the fact that most of the AIMD calculations were run sampling the velocity distributions determined from experiments for $CHD_3$ dissociation on Pt(111)[15] and not those from the Pt(210) measurements presented here. The velocity distributions from both sets of experiments were found to be very similar, and the calculation at an incident energy of 108.1 kJ/mol was run for the velocity distribution determined in this work which fitted well with the trend of the rest of the calculations. From this we conclude that using different velocity distributions to those in the experiments should not significantly affect the calculated sticking coefficients and is probably not the reason for the differences between the data.

An alternative explanation would be that the SRP32-vdW functional fails to accurately describe the interaction potential for methane dissociation on the kinked Pt(210) surface. The calculations with the SRP32-vdW functional overestimating the experimental sticking coefficients suggests that the functional underestimates the minimum activation barrier for the dissociation. It could also model the corrugation of the interaction potential incorrectly. This is reflected in the gradients of the S-shape curves which is related to $W$. The calculated sticking coefficients were fit using eq 6 fixing the values of $A$ and $W$ that were obtained from the experimental fit to determine whether the shape of the curve for the calculated $S_0$ was the same as those from the experiments. This gives an energy shift between the two curves of 13.8 kJ/mol, in good agreement with the average value given above. The calculations yield a steeper curve than the shifted experimental fit (dotted blue line) with the sticking coefficients larger at higher incident energies and smaller at lower incident energies, as shown in Figure 3A. This suggests that both the corrugation of the potential barrier and the

minimum activation barrier for the dissociation of $CHD_3$ on Pt(210) are not correctly described using the SRP32-vdW functional.

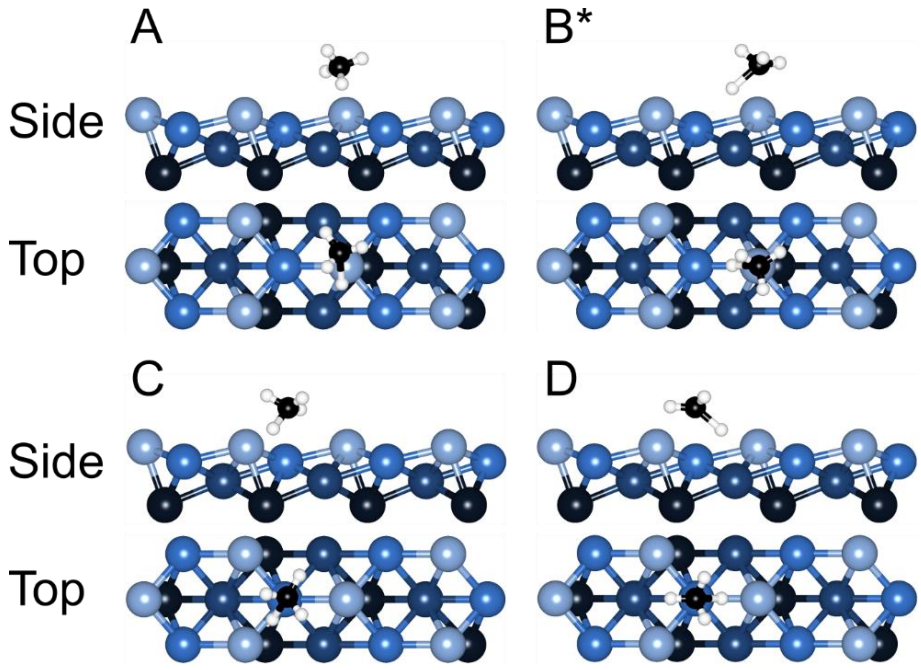


**Figure 4.** Side (first and third row) and top (second and fourth row) views of the transition states found on the kink atom (A and B) and on the middle atom (C and D). The geometries and activation barriers are given in Table 2. The transition state marked with a * has a small second imaginary frequency, i.e., it is not a true first order saddle point.

**Table 2.** The label given in Figure 4, position on the surface, height of the carbon above the Pt(210) plane ($Z_C$), bond length (r), angle between the dissociating bond and surface normal (θ), angle between the umbrella axis and surface normal (β), angle between the dissociating bond and umbrella axis (γ) and activation barriers ($E_b^e$) calculated using eq S3 for the different transition states found for methane dissociation on Pt(210). The transition state marked with a * has a small second imaginary frequency, i.e., it is not a true first order saddle point.

| Label | Atom | $Z_C$ (Å) | r (Å) | θ (°) | β (°) | γ (°) | $E_b^e$ (kJ/mol) |
|---|---|---|---|---|---|---|---|
| A | Kink | 2.13 | 1.58 | 118 | 149 | 32 | 38.7 |
| B* | Kink | 2.22 | 1.59 | 131 | 164 | 32 | 44.6 |
| C | Middle | 1.74 | 1.51 | 128 | 158 | 31 | 100.7 |
| D | Middle | 1.75 | 1.53 | 131 | 162 | 32 | 109.5 |

Figure 4 presents the top (left column) and side (right column) views of the transition states that were calculated for methane dissociating on the kink atom (Panels A and B) and the middle atom (Panels C and D). No transition state was found corresponding to methane dissociation above the bottom atom. The transition states were located using the dimer method as implemented in the VASP transition state tools package[68–71]. In these calculations, the Pt(210) slab was held fixed in its relaxed 0 K geometry while all 15 molecular degrees of freedom were optimized. All the reported transition states correspond to first order saddle points, i.e., there is only one imaginary frequency, except for that shown in Panel B which still has a second small imaginary frequency. The activation barriers, $E_b^e$, were calculated using eq S3 and are reported in Table 2. The lowest activation barrier of 38.7 kJ/mol is found for dissociation on the least coordinated kink atom which corresponds to the transition state shown schematically in Figure 4A. This is lower than the activation barrier on the flat Pt(111)[15] and stepped Pt(211)[15,34] and Pt(110)-(2x1)[33] surfaces reflecting the lower generalized co-ordination number[22,23] of the kink atom than the atoms in the flat and stepped surfaces. We find that the activation barriers for the different surfaces do not depend strictly linearly on the generalized co-ordination number, as shown in Figure S4 of the SI, but rather scatter around a line, in reasonable agreement with the trend in adsorption energies of oxygen and hydrogen adsorbates on Pt nanoparticles[22,23]. The geometry of the transition state with the lowest activation barrier, also given in Table 2, more closely resembles that calculated on the stepped Pt(110)-(2x1)[33] surface than on the flat Pt(111)[25] surface.

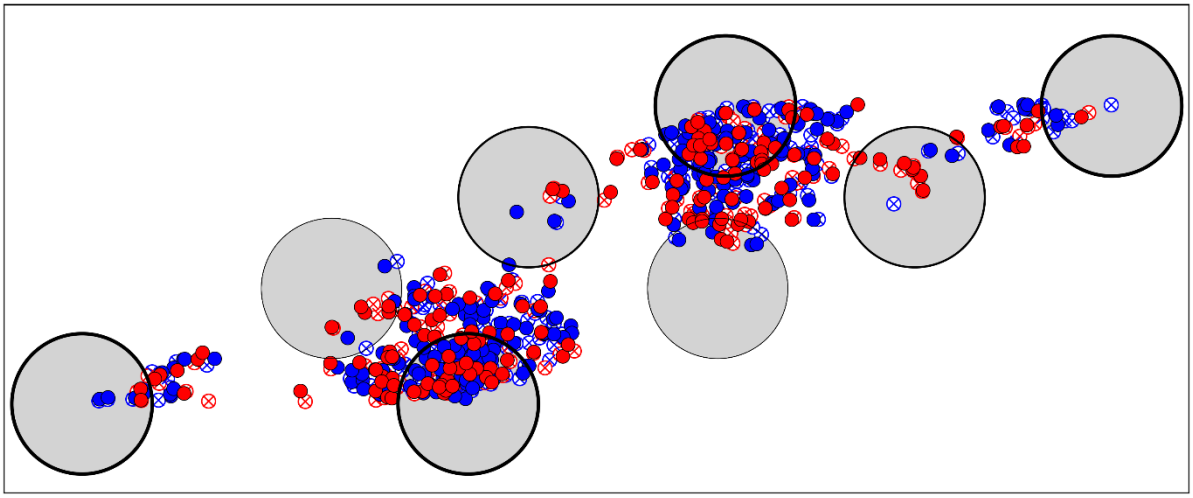

**Figure 5.** The initial positions of the center of mass (COM) of the molecule for all the reacted (blue crossed circles for C-D cleavage and red crossed circles for C-H cleavage) trajectories. The solid symbols show the position of the COM when the C-H bond (red) or C-D bond (blue) becomes larger than the transition state value for the reacted trajectories. The gray circles show the positions of the surface atoms, with those with the thickest outline being the kink (first and fourth row), and those with the thinnest outline the bottom atoms (third row). The second row corresponds to the middle atoms.

The positions of the COM of all the molecules that react, independent of initial incident energy and vibrational state, at the point where the dissociating C-H (red) or C-D (blue) bond becomes larger than the transition state value are shown in Figure 5. The gray circles represent the surface atoms in a (1x1) unit cell; those with the thickest outline (first and fourth rows) correspond to the kink atoms and those with the thinnest outline (third row) the bottom atoms. The second row in the Figure is the middle atoms. Most of the trajectories dissociate over the kink atom, which has the lowest activation barrier. The fraction of molecules that dissociate nearest the kink (red) and middle (blue) atoms is presented in Figure 6 as a function of the incident energy under laser-off conditions (Panel A) and for molecules prepared with a single quantum of C-H stretch vibration (Panel B). No molecules are seen to dissociate nearest the bottom atom. Dissociation nearest the kink atom dominates, although the results suggest that more dissociation is seen on the middle atom for the trajectories where the molecules have a quantum of C-H stretch vibration, and at higher

translational energies. However, these trends are within the error bars of the calculations and could just reflect statistical fluctuations in the data.

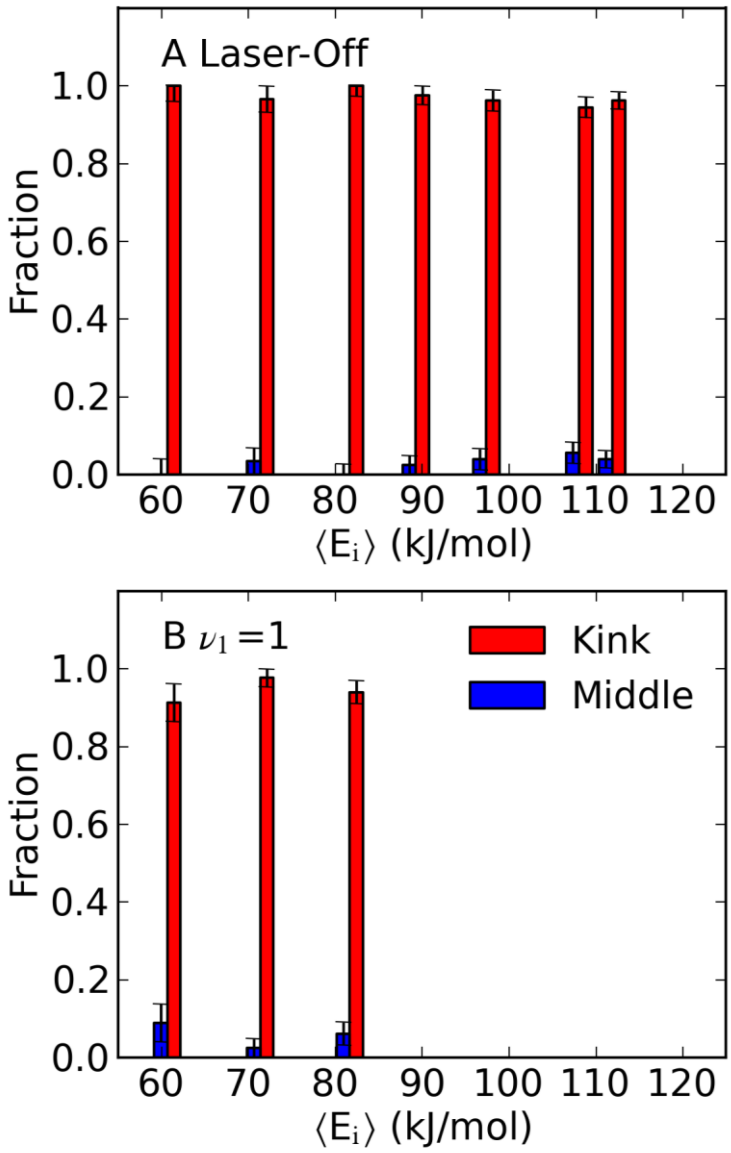


**Figure 6.** Panel A: The fraction of molecules that dissociate on the kink (red) and middle (blue) atoms in the AIMD trajectories under laser-off conditions. Panel B: As for Panel A, but for $CHD_3$ molecules prepared with a quantum of C-H stretch vibration.

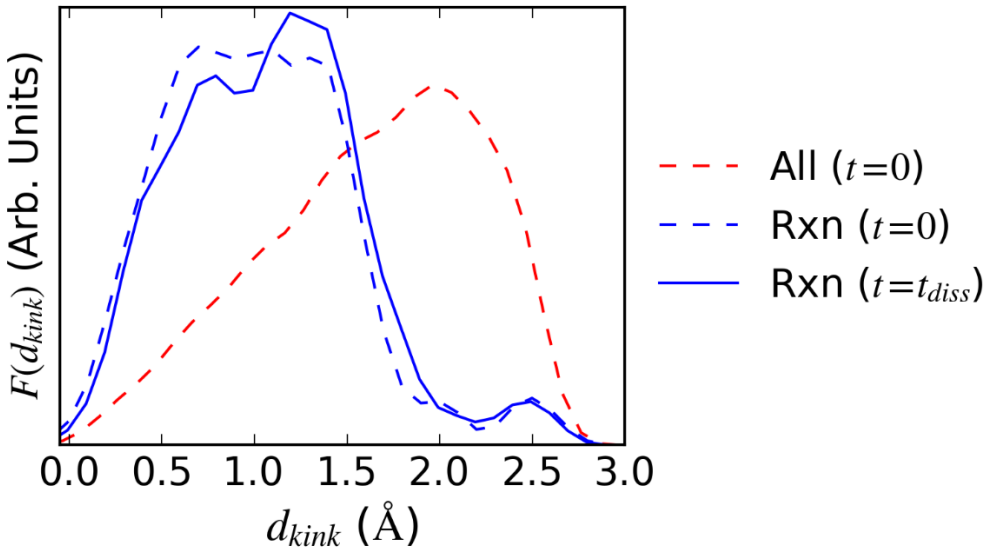


**Figure 7.** The distance of the molecules away from a kink atom in the *XY* plane at the start of all trajectories (red dashed line), at the start of the trajectories where the molecules react (blue dashed line) and at the point where the dissociating bond of the molecules that react becomes larger than the transition state value (blue solid line). All the distributions were calculated using eq 7.

The initial positions of the COM of the molecules that react are also shown in Figure 5 for molecules that dissociate *via* C-H cleavage (red crossed circles) and C-D cleavage (blue crossed circles). This suggests there is little translational steering of the trajectories that dissociate as the $CHD_3$ molecule approaches the Pt(210) surface. The distributions of the distances of the COM of the molecules away from the kink atom in the *XY* plane for all the molecules at the start of the trajectory (red dashed line, $t$ = 0), and for the molecules that react, at the start of the trajectory (blue dashed line, $t$ = 0), and at the time where the dissociating bond becomes longer than the transition state value (blue solid line, $t = t_{diss}$), are presented in Figure 7. These have been calculated using Gaussian binning as[25]

$$F(d_{kink}) \propto \sum_{i}^{N_{bins}} \sum_{j}^{N_{data}} exp\left(-\frac{(b_0 + i\Delta b - d_{kink}(j))^2}{2{\sigma_G}^2}\right) \quad (7)$$

The double summation runs over the number of bins, $N_{bins}$, and the number of data points, $N_{data}$, $b_0$ is the value of the first bin, $\Delta b$ the width of the bin, $d_{kink}(j)$ the distance of the

COM from the kink atom in the *XY* plane for the $j^{th}$ data point and $\sigma_G$ the width of the Gaussian used. For the data presented in Figure 7, $\Delta b = \sigma_G$ = 0.1 Å, and $F(d_{kink})$ have been normalized such that the area is one for each data set. The distributions in the Figure show that there is little translational steering, as $F(d_{kink})$ for the molecules that react are similar at the start of the trajectory and the time of the dissociation. They also indicate that most of the dissociation occurs within 1.5 Å of the site of the kink atoms in the *XY* plane. This is consistent with results for Pt(211) which show that reactivity on the least-coordinated step edge atom dominates[15,25,35,36,40], and on Pt(110)-(2x1) where most reactivity occurs on the ridge atom[33,37].

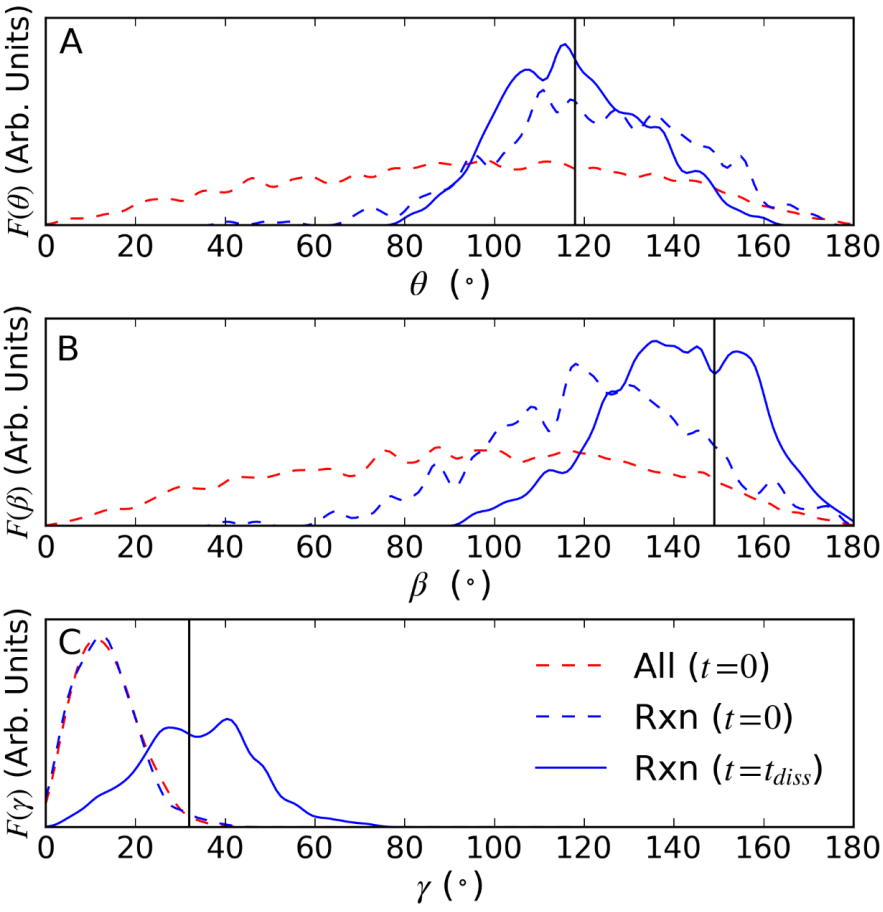


**Figure 8.** Panel A: The initial distribution of θ for all molecules (red dashed line), the initial distribution for those that react (blue dashed line) and the distribution at the point where the dissociating bond in the molecules that react becomes longer than the transition state value (solid blue line). All the distributions were calculated using eq 7. The solid black line shows the transition state value. Panel B: As for panel A, but for β. Panel C: As for panel A, but for γ.

The distributions of the angles that describe the initial geometry of the $CHD_3$ molecule for all the trajectories (red dashed line), the initial geometry of the molecules that react (blue dashed line), and the geometry of the molecules that react at the point where the dissociating bond becomes longer than the transition state value (blue solid line) are presented in Figure 8. Panel A shows the distributions of θ, the angle between the dissociating bond and surface normal, Panel B the distributions of β, the angle between the methyl umbrella axis and surface normal, and Panel C the distributions of γ, the angle between the dissociating bond and the umbrella axis. If the molecule does not react, the angles are defined with respect to the C-H bond axis and the $CD_3$ umbrella axis. The angles are depicted in Figure 7 of Reference 25. The distributions have been calculated using an analogous expression to eq 7 with $\Delta b$ = 1° and $\sigma_G$ = 2° and have been normalized. The initial distributions of θ and β, shown in Panels A and B respectively, are both sine distributions showing that the initial conditions have been correctly sampled. The initial distributions of θ and β for the trajectories that react are similar to the distributions of the angles at the point of reaction, which are positioned around the transition state values shown by black lines, indicating that the molecules that react have to be oriented in a favorable geometry initially and there is little steering during the course of the trajectory. The distribution of θ shifts slightly to smaller values, whereas the distribution of β shifts to larger values, which corresponds to a change in the internal geometry of the $CHD_3$ molecules that react, shown by the change in distributions in γ in Panel C. The same trends have been reported previously for $CHD_3$ dissociation on Pt(111)[25,72], Pt(211)[25] and Pt(110)-(2x1)[33]. The results show that the rotational dynamics of the reacting molecules is closer to the sudden limit than to the rotationally adiabatic limit.

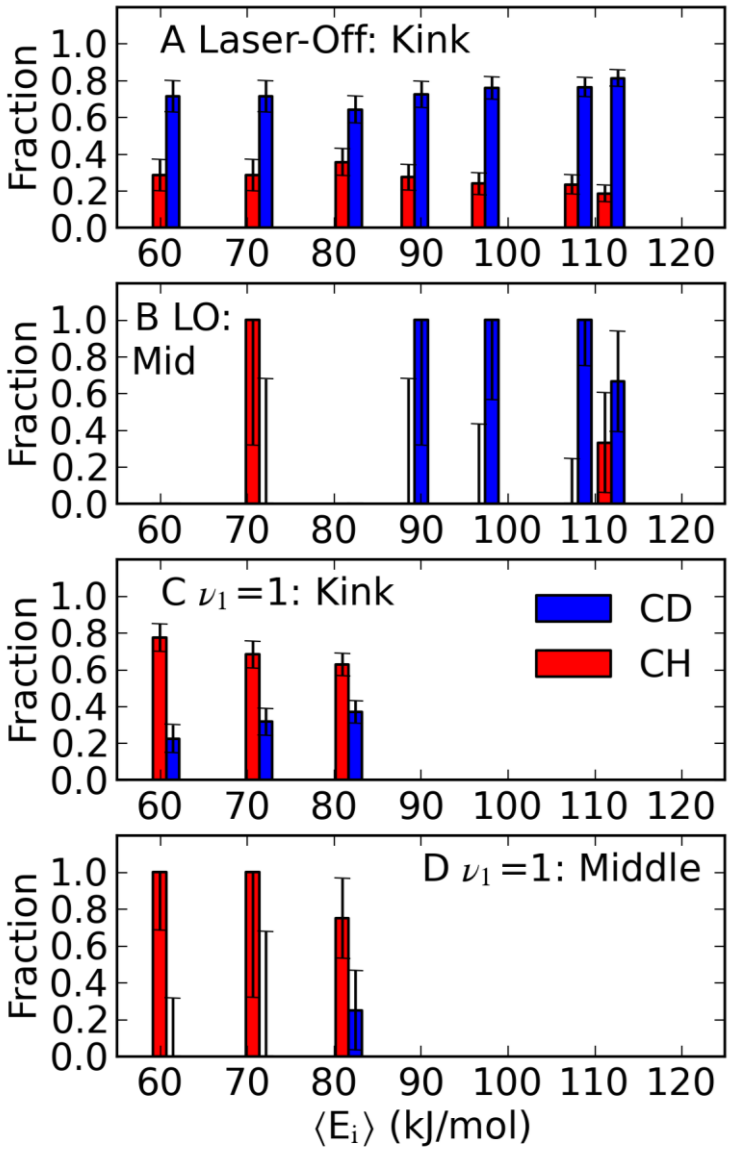


**Figure 9.** Panel A: Fraction of C-H (red) and C-D cleavage (blue) on the kink atom under laser-off conditions. Panel B: Fraction of C-H (red) and C-D cleavage (blue) on the middle (Mid) atom under laser-off (LO) conditions. Panel C: Fraction of C-H (red) and C-D cleavage (blue) on the kink atom for molecules prepared with a quantum of C-H stretch. Panel D: Fraction of C-H (red) and C-D cleavage (blue) on the middle atom for molecules prepared with a quantum of C-H stretch.

Figure 9 presents the fraction of C-H (red) and C-D (blue) cleavage from the AIMD calculations for molecules that dissociate on the kink (Panels A and C) and on the middle atom (Panels B and D) under laser-off conditions (Panels A and B) and for molecules prepared with a quantum of C-H stretch vibration (Panels C and D). In the laser-off calculations, the fraction of C-H cleavage is seen to be 0.25 at all energies for both reaction

sites within error bars, which corresponds to a statistical 3:1 C-D:C-H branching ratio. For the quantum-state resolved calculations with the molecules prepared in the $v_1 = 1$ state, more molecules react *via* C-H cleavage than C-D cleavage. This is more pronounced on the middle atom where the activation barrier is larger, and at lower incident energies where the additional vibrational energy in the C-H bond makes more of a contribution to overcoming the activation barrier to the reaction.

We conclude this section with a comparison of the experimental sticking coefficients (Panel A) and those from AIMD calculations under laser-off conditions (Panel B) and for $CHD_3$ prepared in the $v_1 = 1$ state (Panel C) for dissociation on Pt(111)[15] (black), Pt(211)[15] (red), Pt(110)-(2x1)[33] (green) and Pt(210) (blue) in Figure 10. For Pt(111) the results are for $T_S$ = 500 K whereas for the other surfaces, $T_S$ = 650 K. Previous work for $CH_4$ dissociation on Pt(111) shows that the sticking coefficients at the two surface temperatures are not significantly different[59], meaning this difference will not affect the qualitative discussion presented here. At lower incident energies (< 100 kJ/mol) the AIMD calculations predict a larger increase in sticking coefficients going from the flat to stepped to kinked platinum surfaces than is seen in the experiments, which show the stepped Pt(211) surface has a similar reactivity to the kinked Pt(210) surface. This is in contrast to earlier work[30] which showed that the values of $S_0$ for methane dissociation on kinked Pd(679)[31] were larger than on stepped Pd(311)[30] and on flat Pd(111)[30]. The experiments here do show that the sticking coefficients for $CHD_3$ on Pt(110)-(2x1), which is also stepped, are lower than for the kinked surface and higher than for Pt(111). In the calculations, the Pt(110)-(2x1) surface is the least reactive if there is no contribution to the reactivity from trajectories which result in the $CHD_3$ molecule being trapped on the surface at the end of the 1 ps propagation time. Whilst some of these trapped trajectories may go on to react, it is likely the calculations would still underestimate the measured sticking coefficients. As we have shown, this is most likely due

to the SRP32-vdW functional not correctly producing the correct (experimental) surface structure, which results in the calculated activation barrier being approximately 10 kJ/mol too high[33].

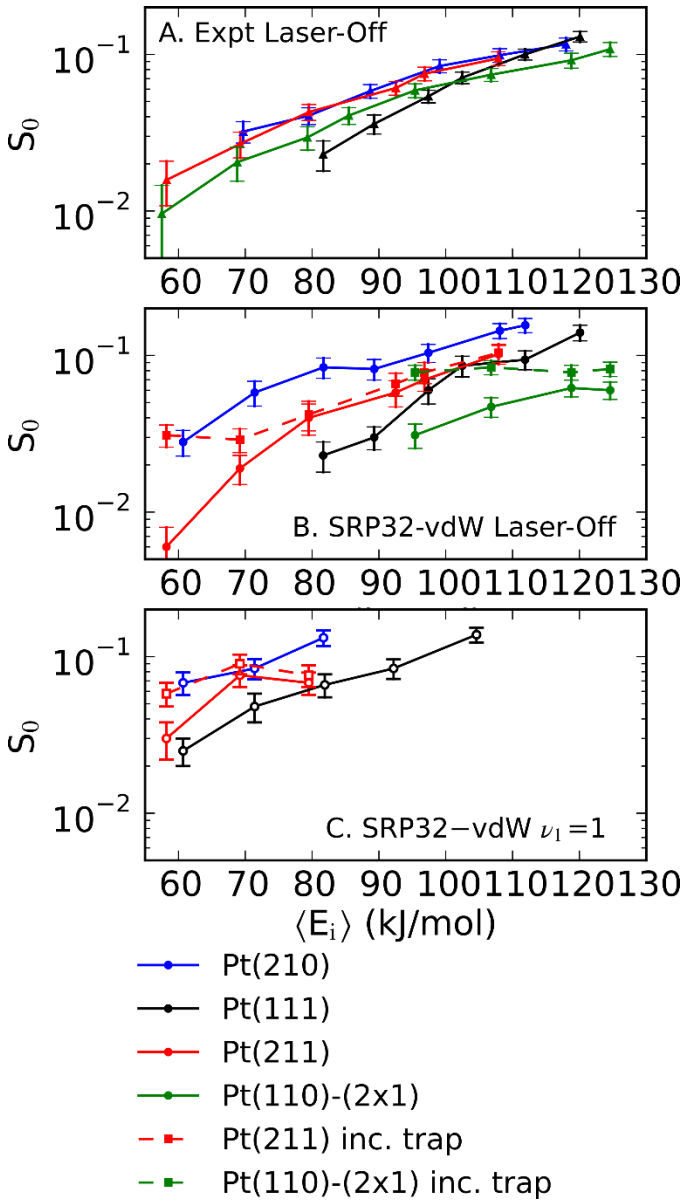


**Figure 10.** Panel A: A comparison of the measured sticking coefficients obtained here for $CHD_3$ dissociation on Pt(210) ($T_S$ = 650 K, blue) under laser-off conditions with those from previous studies on Pt(111)[15] ($T_S$ = 500 K, black), Pt(211)[15] ($T_S$ = 650 K, red) and Pt(110)-(2x1)[33] ($T_S$ = 650 K, green). Lines have been added to guide the eye. Panel B: As for panel A, but results are for AIMD calculations using the SRP32-vdW functional under laser-off conditions. The circles show the sticking coefficients without including a contribution from trapped trajectories, and the squares the sticking coefficients assuming all trapped trajectories react. Panel C: As for panel B, but results are for AIMD calculations using the SRP32-vdW functional for molecules prepared in the $v_1 = 1$ state.

At the highest incident energy, the experiments show the highest reactivity is seen on the Pt(111) surface. The results from the AIMD calculations presented here are likely to follow this trend if extrapolated to higher incident energies, although the cross-over of the Pt(210) and Pt(111) curves would occur at a higher incident energy than in the case of the experiments. This suggests that the AIMD calculations using the SRP32-vdW functional qualitatively model the interplay between the density of the number of sites on the surface with the minimum activation barrier and the height of this barrier, which gives rise to this trend[33]. However, the SRP32-vdW functional only models $CHD_3$ dissociation on Pt(111)[15] and Pt(211)[15] with chemical accuracy; for Pt(110)-(2x1) it underestimates the reactivity[33], and as shown here, for Pt(210) it overestimates the sticking coefficients.

## 5. Conclusions

We have presented a comparison of initial sticking coefficients for $CHD_3$ dissociation on the kinked Pt(210) surface at a temperature of 650 K measured using the King and Wells technique and calculated using AIMD trajectories with the SRP32-vdW functional. The calculations overestimate the experimentally determined values of $S_0$, with the energy shift between the two sets of data being 13.6 kJ/mol. This is over a factor of 3 higher than the 4.2 kJ/mol which defines so-called chemical accuracy, suggesting the SRP32-vdW functional is not transferrable to $CHD_3$ dissociation on the kinked Pt(210) surface. Instead, the functional appears to predict an activation barrier for the reaction that is too low, and to not correctly capture the corrugation of the interaction.

The calculations show that the lowest energy transition state is for dissociation of $CHD_3$ above the kink atom, which has the smallest generalized co-ordination number on the Pt(210) surface. This is also the site where most of the dissociation occurs in the calculations. In addition, the trajectory calculations show that steering effects are unlikely to be significant

in the dissociation of $CHD_3$ on Pt(210), with the molecules that react being oriented in a favorable geometry above a favorable (kink) site at the start of the trajectory. They also suggest that for the trideuterated methane isotopologue considered here, the branching ratio for C-D:C-H cleavage is statistical under laser-off conditions. Molecules prepared with a quantum of C-H stretch excitation preferentially react *via* C-H cleavage, with the effect more pronounced on the middle atom than the kink atom.

## ASSOCIATED CONTENT

### Supporting Information

Generating the Pt(210) surface, convergence tests, residual energy correction, activation barriers and generalized co-ordination numbers, and sticking coefficients.


## ACKNOWLEDGMENTS

We gratefully acknowledge financial support from the Swiss National Science Foundation (grant Nos. P300P2-171247 and 178775/1), the Ecole Polytechnique Fédérale de Lausanne and the European Research Council through an ERC2013 advanced grant (No. 338580) as well as computer time granted by NWO-EW through a Dutch Computing Challenge Project grant.


## AUTHOR INFORMATION


[†]Present address: Department of Chemistry, Swansea University, Singleton Park, Swansea, SA2 8PP, United Kingdom.

**Corresponding author**

Email: h.j.chadwick@swansea.ac.uk

**References**


(1) Chorkendorff, I.; Niemantsverdriet, J. W. *Concepts of Modern Catalysis and Kinetics*; Wiley-VCH: Weinheim, 2003.

(2) Besenbacher, F.; Chorkendorff, I.; Clausen, B. S.; Hammer, B.; Molenbroek, A. M.; Nørskov, J. K.; Stensgaard, I. Design of a Surface Alloy Catalyst for Steam Reforming. *Science.* **1998**, *279*, 1913–1915.

(3) Froment, G. F. Production of Synthesis Gas by Steam- and $CO_2$-Reforming of Natural Gas. *J. Mol. Catal. A Chem.* **2000**, *163*, 147–156.

(4) Bradford, M. C. J.; Vannice, M. A. $CO_2$ Reforming of $CH_4$. *Catal. Rev.* **1999**, *41*, 1–42.

(5) Ashcroft, A. T.; Cheetham, A. K.; Green, M. L. H.; Vernon, P. D. F. Partial Oxidation of Methane to Synthesis Gas Using Carbon Dioxide. *Nature* **1991**, *352*, 225–226.

(6) Zhang, Z. L.; Verykios, X. E. Carbon Dioxide Reforming of Methane to Synthesis Gas over Supported Ni Catalysts. *Catal. Today* **1994**, *21*, 589–595.

(7) Hansen, T. W.; Wagner, J. B.; Hansen, P. L.; Dahl, S.; Topsøe, H.; Jacobsen, C. J. H. Atomic-Resolution in Situ Transmission Electron Microscopy of a Promoter of a Heterogeneous Catalyst. *Science* **2001**, *294*, 1508–1510.

(8) Hansen, P. L.; Wagner, J. B.; Helveg, S.; Rostrup-Nielsen, J. R.; Clausen, B. S.; Topsøe, H. Atom-Resolved Imaging of Dynamic Shape Changes in Supported Copper Nanocrystals. *Science***2002**, *295*, 2053–2055.

(9) Hofmann, S.; Sharma, R.; Ducati, C.; Du, G.; Mattevi, C.; Cepek, C.; Cantoro, M.; Pisana, S.; Parvez, A.; Cervantes-Sodi, F.; et al. In Situ Observations of Catalyst Dynamics during Surface-Bound Carbon Nanotube Nucleation. *Nano Lett.* **2007**, *7*, 602–608.

(10) Gontard, L. C.; Chang, L.-Y.; Hetherington, C. J. D.; Kirkland, A. I.; Ozkaya, D.;

Dunin-Borkowski, R. E. Aberration-Corrected Imaging of Active Sites on Industrial Catalyst Nanoparticles. *Angew. Chemie Int. Edit.* **2007**, *46*, 3683–3685.

(11) Zambelli, T.; Wintterlin, J.; Trost, J.; Ertl, G. Identification of the "Active Sites" of a Surface-Catalyzed Reaction. *Science* **1996**, *273*, 1688–1690.

(12) Hammer, B. Bond Activation at Monatomic Steps: NO Dissociation at Corrugated Ru(0001). *Phys. Rev. Lett.* **1999**, *83*, 3681–3684.

(13) Viñes, F.; Lykhach, Y.; Staudt, T.; Lorenz, M. P. A.; Papp, C.; Steinrück, H.-P.; Libuda, J.; Neyman, K. M.; Görling, A. Methane Activation by Platinum: Critical Role of Edge and Corner Sites of Metal Nanoparticles. *Chem. – A Eur. J.* **2010**, *16*, 6530–6539.

(14) Nørskov, J. K.; Bligaard, T.; Hvolbæk, B.; Abild-Pedersen, F.; Chorkendorff, I.; Christensen, C. H. The Nature of the Active Site in Heterogeneous Metal Catalysis. *Chem. Soc. Rev.* **2008**, *37*, 2163–2171.

(15) Migliorini, D.; Chadwick, H.; Nattino, F.; Gutiérrez-González, A.; Dombrowski, E.; High, E. A.; Guo, H.; Utz, A. L.; Jackson, B.; Beck, R. D.; et al. Surface Reaction Barriometry: Methane Dissociation on Flat and Stepped Transition Metal Surfaces. *J. Phys. Chem. Lett.* **2017**, *8*, 4177–4182.

(16) Wolcott, C. A.; Medford, A. J.; Studt, F.; Campbell, C. T. Degree of Rate Control Approach to Computational Catalyst Screening. *J. Catal.* **2015**, *330*, 197–207.

(17) Xu, Y.; Lausche, A. C.; Wang, S.; Khan, T. S.; Abild-Pedersen, F.; Studt, F.; Nørskov, J. K.; Bligaard, T. *In Silico* Search for Novel Methane Steam Reforming Catalysts. *New J. Phys.* **2013**, *15*, 125021.

(18) Guo, H.; Menzel, J. P.; Jackson, B. Quantum Dynamics Studies of the Dissociative Chemisorption of $CH_4$ on the Steps and Terraces of Ni(211). *J. Chem. Phys.* **2018**, *149*, 244704.

(19) Medford, A. J.; Vojvodic, A.; Hummelshøj, J. S.; Voss, J.; Abild-Pedersen, F.; Studt, F.; Bligaard, T.; Nilsson, A.; Nørskov, J. K. From the Sabatier Principle to a Predictive Theory of Transition-Metal Heterogeneous Catalysis. *J. Catal.* **2015**, *328*, 36–42.

(20) Latimer, A. A.; Kulkarni, A. R.; Aljama, H.; Montoya, J. H.; Yoo, J. S.; Tsai, C.; Abild-Pedersen, F.; Studt, F.; Nørskov, J. K. Understanding Trends in C–H Bond Activation in Heterogeneous Catalysis. *Nat. Mater.* **2017**, *16*, 225–229.

(21) Wang, S.; Petzold, V.; Tripkovic, V.; Kleis, J.; Howalt, J. G.; Skűlason, E.; Fernández, E. M.; Hvolbæk, B.; Jones, G.; Toftelund, A.; et al. Universal Transition State Scaling Relations for (De)Hydrogenation over Transition Metals. *Phys. Chem. Chem. Phys.* **2011**, *13*, 20760–20765.

(22) Calle- Vallejo, F.; Martínez, J. I.; García- Lastra, J. M.; Sautet, P.; Loffreda, D. Fast Prediction of Adsorption Properties for Platinum Nanocatalysts with Generalized Coordination Numbers. *Angew. Chemie Int. Edit.* **2014**, *53*, 8316–8319.

(23) Calle-Vallejo, F.; Tymoczko, J.; Colic, V.; Vu, Q. H.; Pohl, M. D.; Morgenstern, K.; Loffreda, D.; Sautet, P.; Schuhmann, W.; Bandarenka, A. S. Finding Optimal Surface Sites on Heterogeneous Catalysts by Counting Nearest Neighbors. *Science* **2015**, *350*, 185–189.

(24) Van Santen, R. A. Complementary Structure Sensitive and Insensitive Catalytic Relationships. *Acc. Chem. Res.* **2009**, *42*, 57–66.

(25) Migliorini, D.; Chadwick, H.; Kroes, G. J. Methane on a Stepped Surface: Dynamical Insights on the Dissociation of $CHD_3$ on Pt(111) and Pt(211). *J. Chem. Phys.* **2018**, *149*, 094701.

(26) Nave, S.; Tiwari, A. K.; Jackson, B. Methane Dissociation and Adsorption on Ni(111), Pt(111), Ni(100), Pt(100), and Pt(110)-(1×2): Energetic Study. *J. Chem. Phys.* **2010**, *132*, 054705.

(27) Beebe, T. P.; Goodman, D. W.; Kay, B. D.; Yates, J. T. Kinetics of the Activated Dissociative Adsorption of Methane on the Low Index Planes of Nickel Single Crystal Surfaces. *J. Chem. Phys.* **1987**, *87*, 2305–2315.

(28) Egeberg, R. C.; Ullmann, S.; Alstrup, I.; Mullins, C. B.; Chorkendorff, I. Dissociation of $CH_4$ on Ni(111) and Ru(0001). *Surf. Sci.* **2002**, *497*, 183–193.

(29) Abild-Pedersen, F.; Lytken, O.; Engbæk, J.; Nielsen, G.; Chorkendorff, I.; Nørskov, J. K. Methane Activation on Ni(111): Effects of Poisons and Step Defects. *Surf. Sci.* **2005**, *590*, 127–137.

(30) Klier, K.; Hess, J. S.; Herman, R. G. Structure Sensitivity of Methane Dissociation on Palladium Single Crystal Surfaces. *J. Chem. Phys.* **1997**, *107*, 4033–4043.

(31) Nan,Y.-W.; Herman, R. G.; Klier, K. Dissociative Adsorption of Methane on Pd(679) Surface. *Surf. Sci.* **1992**, *279*, 33–48.

(32) Gee, A. T.; Hayden, B. E.; Mormiche, C.; Kleyn, A. W.; Riedmüller, B. The Dynamics of the Dissociative Adsorption of Methane on Pt(533). *J. Chem. Phys.* **2003**, *118*, 3334–3341.

(33) Chadwick, H.; Gutiérrez-González, A.; Beck, R. D.; Kroes, G. J. Transferability of the SRP32-VdW Specific Reaction Parameter Functional to $CHD_3$ Dissociation on Pt(110)-(2x1). *J. Chem. Phys.* **2019**, *150*, 124702.

(34) Migliorini, D.; Chadwick, H.; Nattino, F.; Gutiérrez-González, A.; Dombrowski, E.; High, E. A.; Guo, H.; Utz, A. L.; Jackson, B.; Beck, R. D.; et al. Correction to "Surface Reaction Barriometry: Methane Dissociation on Flat and Stepped Transition-Metal Surfaces." *J. Phys. Chem. Lett.* **2019**, *10*, 661–662.

(35) Chadwick, H.; Guo, H.; Gutiérrez-González, A.; Menzel, J. P.; Jackson, B.; Beck, R. D. Methane Dissociation on the Steps and Terraces of Pt(211) Resolved by Quantum State and Impact Site. *J. Chem. Phys.* **2018**, *148*, 014701.

(36) Gutiérrez-González, A.; Crim, F. F.; Beck, R. D. Bond Selective Dissociation of Methane ($CH_3D$) on the Steps and Terraces of Pt(211). *J. Chem. Phys.* **2018**, *149*, 074701.

(37) Gutiérrez-González, A.; Torio, M. E.; Busnengo, H. F.; Beck, R. D. Site Selective Detection of Methane Dissociation on Stepped Pt Surfaces. *Top. Catal.* https://doi.org/10.1007/s11244-019-01170-5

(38) Nattino, F.; Migliorini, D.; Kroes, G. J.; Dombrowski, E.; High, E. A.; Killelea, D. R.; Utz, A. L. Chemically Accurate Simulation of a Polyatomic Molecule-Metal Surface Reaction. *J. Phys. Chem. Lett.* **2016**, *7*, 2402–2406.

(39) Zhou, X.; Nattino, F.; Zhang, Y.; Chen, J.; Kroes, G. J.; Guo, H.; Jiang, B. Dissociative Chemisorption of Methane on Ni(111) Using a Chemically Accurate Fifteen Dimensional Potential Energy Surface. *Phys. Chem. Chem. Phys.* **2017**, *19*, 30540–30550.

(40) Chadwick, H.; Gutiérrez-González, A.; Migliorini, D.; Beck, R. D.; Kroes, G. J. Incident Angle Dependence of $CHD_3$ Dissociation on the Stepped Pt(211) Surface. *J. Phys. Chem. C* **2018**, *122*, 19652–19660.

(41) Kresse, G.; Hafner, J. *Ab Initio* Molecular-Dynamics Simulation of the Liquid-Metal–amorphous-Semiconductor Transition in Germanium. *Phys. Rev. B* **1994**, *49*, 14251–14269.

(42) Kresse, G.; Hafner, J. *Ab Initio* Molecular Dynamics for Liquid Metals. *Phys. Rev. B* **1993**, *47*, 558–561.

(43) Kresse, G.; Furthmüller, J. Efficient Iterative Schemes for *Ab Initio* Total-Energy Calculations Using a Plane-Wave Basis Set. *Phys. Rev. B* **1996**, *54*, 11169–11186.

(44) Kresse, G.; Furthmüller, J. Efficiency of *Ab-Initio* Total Energy Calculations for Metals and Semiconductors Using a Plane-Wave Basis Set. *Comp. Mater. Sci.* **1996**, *6*,

15–50.

(45) Kresse, G.; Joubert, D. From Ultrasoft Pseudopotentials to the Projector Augmented-Wave Method. *Phys. Rev. B* **1999**, *59*, 1758–1775.

(46) Blöchl, P. E. Projector Augmented-Wave Method. *Phys. Rev. B* **1994**, *50*, 17953–17979.

(47) Perdew, J. P.; Burke, K.; Ernzerhof, M. Generalized Gradient Approximation Made Simple. *Phys. Rev. Lett.* **1996**, *77*, 3865–3868.

(48) Perdew, J. P.; Burke, K.; Ernzerhof, M. Generalized Gradient Approximation Made Simple [Phys. Rev. Lett. 77, 3865 (1996)]. *Phys. Rev. Lett.* **1997**, *78*, 1396.

(49) Gerrits, N.; Migliorini, D.; Kroes, G. J. Dissociation of $CHD_3$ on Cu(111), Cu(211), and Single Atom Alloys of Cu(111). *J. Chem. Phys.* **2018**, *149*, 224701.

(50) Hammer, B.; Hansen, L. B.; Nørskov, J. K. Improved Adsorption Energetics within Density-Functional Theory Using Revised Perdew-Burke-Ernzerhof Functionals. *Phys. Rev. B* **1999**, *59*, 7413–7421.

(51) Dion, M.; Rydberg, H.; Schröder, E.; Langreth, D. C.; Lundqvist, B. I. Van Der Waals Density Functional for General Geometries. *Phys. Rev. Lett.* **2004**, *92*, 246401.

(52) Román-Pérez, G.; Soler, J. M. Efficient Implementation of a van Der Waals Density Functional: Application to Double-Wall Carbon Nanotubes. *Phys. Rev. Lett.* **2009**, *103*, 096102.

(53) Simpson, W. R.; Rakitzis, T. P.; Kandel, S. A.; Orr- Ewing, A. J.; Zare, R. N. Reaction of Cl with Vibrationally Excited $CH_4$ and $CHD_3$: State- to- state Differential Cross Sections and Steric Effects for the HCl Product. *J. Chem. Phys.* **1995**, *103*, 7313–7335.

(54) Louis, T. A. Confidence Intervals for a Binomial Parameter after Observing No Successes. *Am. Stat.* **1981**, *35*, 154.

(55) Chen, L.; Ueta, H.; Bisson, R.; Beck, R. D. Quantum State-Resolved Gas⁄surface Reaction Dynamics Probed by Reflection Absorption Infrared Spectroscopy. *Rev. Sci. Instrum.* **2013**, *84*, 053902.

(56) Sander, M.; Imbihl, R.; Schuster, R.; Barth, J. V; Ertl, G. Microfacetting of Pt(210) Induced by Oxygen Adsorption and by Catalytic CO Oxidation. *Surf. Sci.* **1992**, *271*, 159–169.

(57) Gladys, M. J.; Ermanoski, I.; Jackson, G.; Quinton, J. S.; Rowe, J. E.; Madey, T. E. A High Resolution Photoemission Study of Surface Core-Level Shifts in Clean and Oxygen-Covered Ir(2 1 0) Surfaces. *J. Electron Spectros. Relat. Phenomena* **2004**, *135*, 105–112.

(58) King, D. A.; Wells, M. G. Molecular Beam Investigation of Adsorption Kinetics on Bulk Metal Targets: Nitrogen on Tungsten. *Surf. Sci.* **1972**, *29*, 454–482.

(59) Chadwick, H.; Gutiérrez-González, A.; Beck, R. D. Quantum State Resolved Molecular Beam Reflectivity Measurements: $CH_4$ Dissociation on Pt(111). *J. Chem. Phys.* **2016**, *145*, 174707.

(60) Luntz, A. C. A Simple Model for Associative Desorption and Dissociative Chemisorption. *J. Chem. Phys.* **2000**, *113*, 6901–6905.

(61) Puisto, S. R.; Held, G.; Ranea, V.; Jenkins, S. J.; Mola, E. E.; King, D. A. The Structure of the Chiral Pt{531} Surface: A Combined LEED and DFT Study. *J. Phys. Chem. B* **2005**, *109*, 22456–22462.

(62) Pratt, S. J.; Jenkins, S. J.; King, D. A. The Symmetry and Structure of Crystalline Surfaces. *Surf. Sci.* **2005**, *585*, L159–L165.

(63) Zhang, X.-G.; Van Hove, M. A.; Somorjai, G. A.; Rous, P. J.; Tobin, D.; Gonis, A.; MacLaren, J. M.; Heinz, K.; Michl, M.; Lindner, H.; et al. Efficient Determiniation of Multilayer Relaxation in the Pt(210) Stepped and Densely Kinked Surface. *Phys. Rev.*

*Lett.* **1991**, *67*, 1298–1301.

(64) Klimeš, J.; Bowler, D. R.; Michaelides, A. Van Der Waals Density Functionals Applied to Solids. *Phys. Rev. B* **2011**, *83*, 195131.

(65) Fery, P.; Moritz, W.; Wolf, D. Structure Determination of the (1x2) and (1x3) Reconstructions of Pt(110) by Low-Energy Electron Diffraction. *Phys. Rev. B* **1988**, *38*, 7275–7286.

(66) Sowa, E. C.; Van Hove, M. A.; Adams, D. L. The Missing-Row Model for the Reconstructed Pt(110)−(1 × 2) Surface: A Leed Intensity Analysis Showing Multilayer Distortions. *Surf. Sci.* **1988**, *199*, 174–182.

(67) Fenter, P.; Gustafsson, T. Structural Analysis of the Pt(110)-(1x2) Surface Using Medium-Energy Ion Scattering. *Phys. Rev. B* **1988**, *38*, 10197–10204.

(68) Xiao, P.; Sheppard, D.; Rogal, J.; Henkelman, G. Solid-State Dimer Method for Calculating Solid-Solid Phase Transitions. *J. Chem. Phys.* **2014**, *140*, 174104.

(69) Kästner, J.; Sherwood, P. Superlinearly Converging Dimer Method for Transition State Search. *J. Chem. Phys.* **2008**, *128*, 014106.

(70) Heyden, A.; Bell, A. T.; Keil, F. J. Efficient Methods for Finding Transition States in Chemical Reactions: Comparison of Improved Dimer Method and Partitioned Rational Function Optimization Method. *J. Chem. Phys.* **2005**, *123*, 224101.

(71) Henkelman, G.; Jónsson, H. A Dimer Method for Finding Saddle Points on High Dimensional Potential Surfaces Using Only First Derivatives. *J. Chem. Phys.* **1999**, *111*, 7010–7022.

(72) Nattino, F.; Ueta, H.; Chadwick, H.; Reijzen, M. E. van; Beck, R. D.; Jackson, B.; van Hemert, M. C.; Kroes, G. J. Ab Initio Molecular Dynamics Calculations versus Quantum-State- Resolved Experiments on $CHD_3$ + Pt(111): New Insights into a Prototypical Gas − Surface Reaction. *J. Phys. Chem. Lett.* **2014**, *5*, 1294–1299.

**TOC Graphic**